HAL
open science

Electro-optic properties of ZrO 2 , HfO 2 and LiNbO 3 ferroelectric phases: A comprehensive and comparative study with density functional theory

Ali El Boutaybi, Panaghiotis Karamanis, T Maroutian, Sylvia Matzen, Laurent Vivien, Philippe Lecoeur, Michel Rérat

To cite this version:

Ali El Boutaybi, Panaghiotis Karamanis, T Maroutian, Sylvia Matzen, Laurent Vivien, et al.. Electro-optic properties of ZrO 2 , HfO 2 and LiNbO 3 ferroelectric phases: A comprehensive and comparative study with density functional theory. 2022. hal-03864160

HAL Id: hal-03864160

https://hal.science/hal-03864160v1

Preprint submitted on 21 Nov 2022

HAL is a multi-disciplinary open access archive for the deposit and dissemination of scientific research documents, whether they are published or not. The documents may come from teaching and research institutions in France or abroad, or from public or private research centers.

L'archive ouverte pluridisciplinaire **HAL**, est destinée au dépôt et à la diffusion de documents scientifiques de niveau recherche, publiés ou non, émanant des établissements d'enseignement et de recherche français ou étrangers, des laboratoires publics ou privés.

arXiv:2209.12536v1 [cond-mat.mtrl-sci] 26 Sep 2022

Electro-optic properties of ZrO_2, HfO_2 and $LiNbO_3$ ferroelectric phases: A comprehensive and comparative study with density functional theory

Ali El Boutaybi[1], Panagiotis Karamanis[2], Thomas Maroutian[1], Sylvia Matzen[1], Laurent Vivien[1], Philippe Lecoeur[1], and Michel Rérat[2]

[1]Centre de Nanosciences et de Nanotechnologies (C2N), Universite Paris-Saclay, CNRS, 91120 Palaiseau, France
[2]Institut des Sciences Analytiques et de Physico-Chimie pour l'Environnement et les Matériaux, CNRS, Université de Pau et des Pays de l'Adour, 64053 Pau, France
ali.el-boutaybi@c2n.upsaclay.fr

16 September 2022

Abstract

We report the Pockels electro-optic properties of ZrO_2 and HfO_2 orthorhombic $Pbc2_1$ and rhombohedral R3m ferroelectric phases, and we compare them to the well-known $LiNbO_3$ Pockels material from density functional theory calculations using the CRYSTAL suite of program. Specifically, three essential processes are explicitly investigated: The electronic, the ionic (or vibrational), and the piezoelectric contributions. Our calculations reveal that the ionic part coming from the low-frequency phonon modes contributes the most to the electro-optic coefficients of rhombohedral $LiNbO_3$ and of orthorhombic ZrO_2 and HfO_2. While these low-frequency modes show zero contribution to Pockels coefficients for the rhombohedral phase of the latter compounds.

1 Introduction

Silicon photonics platforms are becoming indispensable for developing low-cost integrated photonic circuits. Electro-optic (EO) effect is one of the main properties required in plethora applications including optical communications [1–4], quantum computing [5, 6], and neuromorphic applications [7–9]. The principal physical process behind these applications is the so-called Pockels or linear EO effect, which is related to the modulation of the refractive index of a material

under an applied external electric field [10]. Nevertheless, due to its centrosymmetric atomistic crystalline structure, pristine silicon features vanishing second-order optical nonlinearities; thus, it is unsuitable for EO applications. Bearing in mind that second-order nonlinear optical (NLO) responses strictly manifest in non-centrosymmetric materials, ferroelectric (FE) crystalline solids have emerged as the main materials of choice in EO applications. Such materials exhibit an intrinsic electric polarization that, in addition, can be controlled and tuned in a reversible manner by the application of an external electric field.

In the realm of EO applications, the most studied FE materials are currently ABO_3 perovskite-type crystalline solids. A representative member of this family is lithium niobate ($LiNbO_3$, LNO), a ferroelectric material featuring a strong Pockels crystalline bulk coefficient (r_{33}) of about 30 pm/V [11]. LNO is widely applied in the telecommunications industry [12] and specifically in the fabrication of optical modulators. Despite LNO's complexity of integration on silicon substrates, several studies showed its compatibility with silicon photonics [13,14]. An additional appealing perovskite-type crystalline solid for EO applications is tetragonal ferroelectric barium titanate ($BaTiO_3$, BTO), featuring one of the highest Pockels bulk coefficients ($r_{42} \approx 1300$ pm/V) [15]. However, the growth of high-quality BTO thin films on silicon without affecting its strong Pockels coefficient is still challenging and of high cost, although high-quality BTO films can be fabricated via molecular beam epitaxy (MBE), [4, 16, 17]. In addition to tetragonal BTO, its rhombohedral R3m phase also gained attention for cryogenic technologies as, for instance, for quantum computing [18, 19].

Recently, it has been demonstrated that among HfO_2-ZrO_2-based thin films, orthorhombic $Pbc2_1$ [20] and rhombohedral R3m [21] phases exhibit ferroelectric behavior. This is a significant outcome in terms of practical applications because both HfO_2 and ZrO_2 have an excellent silicon compatibility [22–25]. Combined with their ferroelectric nature, this might lead to significant breakthroughs in the realm of integrated photonic circuits that could significantly reduce the fabrication cost. Nevertheless, there is still much work to be done since the film quality and the ferroelectricity of ZrO_2 and HfO_2 are not well optimized at high film thicknesses. This is critical for their optimal application due to the inverse proportionality between the optical losses and the film thickness [26, 27]. In the case of the orthorhombic $Pbc2_1$ (o−phase), which is usually reported in polycrystalline thin films, ferroelectricity has been demonstrated in a large range of thickness from 1 nm to 1μm [28–31]. This o−phase has also been reported in epitaxial thin films with a thickness thinner than 20 nm [32–34]. Regarding the rhombohedral R3m (r−phase), the reported thicknesses are ranged from 5 to 40 nm [21, 35, 36]. Indeed, for applications, ultrathin films are often advantageous; for example, in the case of nonvolatile memories and ferroelectric field-effect transistors [22, 23], energy storage [24, 25], negative capacitance [37, 38], and tunnel junctions [39, 40].

In terms of NLO properties, the studies on ZrO_2-HfO_2 materials are scarce, leaving open the question of the potential of these compounds for optical applications. Indeed, to our knowledge, only two experimental studies can be found in the literature [41, 42]. They investigate the EO effect in Y_2O_3-doped HfO_2, reporting an EO coefficient of about 0.67 pm/V for (111)-oriented thin-films, a modest value compared to the ones in LNO and BTO materials. However, the exact EO coefficients of the two experimentally reported ferroelectric phases in HfO_2 and ZrO_2 are not known yet. Therefore, this study's primary objective is to report and investigate the EO coefficients of HfO_2 and ZrO_2

materials.

In this work, we study the second-order nonlinear optical (NLO) properties of the orthorhombic $Pbc2_1$ and rhombohedral R3m phases of ZrO_2 and HfO_2, relying on all-electron density functional theory (DFT) computations to report reliable EO coefficients. The obtained results are compared to the ones computed for the rhombohedral R3c $LiNbO_3$ (LNO) phase, for which experimental data are available allowing us to use LNO as a reference material. All reported EO coefficients have been determined from the microscopic second-order NLO responses of these systems that, in turn, they have been obtained via a coupled perturbed Kohn-Sham (CPKS) analytical approach developed and implemented in the CRYSTAL17 suite of quantum chemical programs by one of the authors of this study [43, 44]. It has already been established that this perturbative approach delivers high accuracy molecular and bulk electric properties, free from numerical errors [45–49]. To achieve the maximum possible relevance with the available or future experimental data, the reported coefficients comprise electronic, vibrational effects, and piezoelectric contributions, which have also been obtained analytically. Especially for comparison between theory and experiment, such contributions are of essential importance for a reliable prediction of the overall NLO response of a given crystalline or molecular material and the complete understanding of its origin.
Our article is organized as follows: First, we give the theoretical background of our study, insisting on the close relationship between the macroscopic NLO susceptibilities and the microscopic hyper-polarizabilities of the unit shells. Then, we study the EO properties of LNO using CRYSTAL code, which will serve as the material of reference. Specifically, we report reliable values of its microscopic second-order responses and analyze the electronic, vibrational, and piezoelectric contributions. Finally, we report and discuss the Pockels EO coefficients of o− and r−phase ZrO_2 and HfO_2, comparing them to those calculated for the R3c rhombohedral phase of LNO.

2 Theoretical framework and computational details

The microscopic linear and non−linear optical properties of a finite zero-dimensional system are defined in terms of a Taylor power series expansion with respect to an external applied electric field E_{jkl} as

$$\mu_i = \mu_0 + \alpha^{tot}_{ij} E_j + \frac{1}{2}\beta^{tot}_{ijk} E_j E_k + \frac{1}{6}\gamma^{tot}_{ijkl} E_j E_k E_l + ... \tag{1}$$

Where, i, j, k and l stand for Cartesian coordinates (x, y, z) , μ_i and μ_0 are the induced and the permanent dipole moment, α^{tot}_{ij} is the total dipole electric polarizability, while β^{tot}_{ijk} and γ^{tot}_{ijkl} are the total first and second dipole hyperpolarizabilities, respectively. By the term total (*tot*) it is implied that both electronic (*ele*) and vibrational (*vib*) contributions [48–50] are taken into account, Hence:

$$\alpha^{tot}_{ij} = \alpha^{ele}_{ij} + \alpha^{vib}_{ij} \tag{2}$$

$$\beta^{tot}_{ijk} = \beta^{ele}_{ijk} + \beta^{vib}_{ijk} \tag{3}$$

For three-dimensional periodic crystalline lattices, equation (1) can be written as

$$P_i = P_0 + \chi^{(1)}_{ij} E_j + \chi^{(2)}_{ijk} E_j E_k + \chi^{(3)}_{ijkl} E_j E_k E_l + ... \tag{4}$$

Where P_i is the unit-cell induced polarization while $\chi^{(1)}_{ij}$, $\chi^{(2)}_{ijk}$, and $\chi^{(3)}_{ijkl}$ stand for the total first order (linear), and the second-and the third-order (nonlinear) optical macroscopic bulk susceptibilities, respectively. The first and second coefficients of equation (4) are deduced from the total microscopic (hyper) polarizabilities per unit-cell volume (V) as follows (in atomic units):

$$\chi^{(1)}_{ij} = \frac{4\pi}{V}\alpha^{tot}_{ij} \tag{5}$$

$$\chi^{(2)}_{ijk} = \frac{2\pi}{V}\beta^{tot}_{ijk} \tag{6}$$

The total first-order susceptibility $\chi^{(1)}_{ij}$ can be used to deduce the relative dielectric tensor ϵ_{ij}, which in turn gives access to bulk refractive indices n via the following expressions:

$$\epsilon_{ij} = \delta_{ij} + \chi^{(1)}_{ij} \tag{7}$$

$$n_{ii} = \epsilon^{1/2}_{ii} \tag{8}$$

In the above equations, δ_{ij} represents the elements of the identity matrix ($\delta_{ij} = 1$ for $i = j$, and 0 for $i \neq j$). Note that we consider in this work a diagonal ϵ_{ij} tensor so that the subscript i of ϵ_{ii} corresponds to one of the three principal axes n_{ii} of the ellipsoidal indicatrix.

Now, to obtain the EO Pockels coefficients (r_{ijk}), as a first step, we consider the constant stress (or "clamped") conditions, wherein $\chi^{(2)}_{ijk}$ and the bulk refractive indices n_{ii} given in equation (8) can be used to determine one out of the two terms contributing to the total r_{ijk} coefficients. The clamped EO coefficient is denoted here as r^S_{ijk}, comprises both vibrational and electronic contributions, and is defined as:

$$r^S_{ijk} = -2\,\frac{\chi^{(2)}_{ijk}}{n^2_{ii}n^2_{jj}} \tag{9}$$

In the second step, we should model and consider the relevant acoustic contribution stemming from the piezoelectric effect. This effect depends on the frequency of the applied ac electric field, as it originates from the inverse piezoelectric effect, according to which the application of an ac oscillating field induces mechanical deformations on the crystalline lattice. The resulting contribution to the r_{ijk} coefficients, denoted here as r^p_{ijk}, is defined from the photoelastic tensor $P_{ij\mu\nu}$ and converse piezoelectric tensor $d_{k\mu\nu}$ [51,52] as:

$$r^p_{ijk} = \sum_{\mu,\nu=1}^{3} P_{ij\mu\nu}d_{k\mu\nu} \tag{10}$$

The calculation of the tensorial components of r^p_{ijk} is achieved via the computation of the photoelastic constants $\frac{\partial\eta_{ij}}{\partial S_{\mu\nu}}$ ($P_{ij\mu\nu}$) defined as the derivative of the impermeability tensor η_{ij} with respect to strain $S_{\mu\nu}$, which are the elements of the fourth rank photoelastic tensor, and of the converse

piezoelectric tensor $\frac{\partial S_{\mu\nu}}{\partial E_k}$ $(d_{k\mu\nu})$ [53]. Finally, the total EO coefficients that we report in this work are calculated as $r_{ijk} = r^S_{ijk} + r^p_{ijk}$. More detailed information about photoelastic calculations can be found elsewhere [51–53].

All computations of frequency-dependent properties have been performed with the CRYSTAL suite of programs [44]. In order to determine the dynamic vibrational and electronic (clamped nuclei) hyper-polarizabilities, a fully analytical approach relying on the coupled perturbed Hartree-Fock and Kohn-Sham method (CPHF / CPKS) has been applied [47–49,54,55]. In the case of LNO, we considered three different DFT functionals to investigate the dependence on the DFT method of the properties of interest and to compare the results with available experimental data. That includes the Becke, three-parameter, Lee-Yang–Parr exchange-correlation functional (B3LYP) [56, 57], the pure Perdew-Burke-Ernzerhof one (PBE) [58], and with 25% Hartree-Fock (HF) exchange (PBE0) [59]. In the case of ZrO_2 and HfO_2 (orthorhombic $Pbc2_1$ and rhombohedral R3m phases), only the B3LYP functional has been applied as it gives good results for LNO. The basis sets of LNO are taken from Refs. [60], [61], and [62] for Nb, Li, and O, respectively. The basis sets for ZrO_2 are from Refs. [61] and [63] for O and Zr, respectively, while those for HfO_2 are taken from Refs. [64] and [65] for O and Hf, respectively.

3 Results and discussion

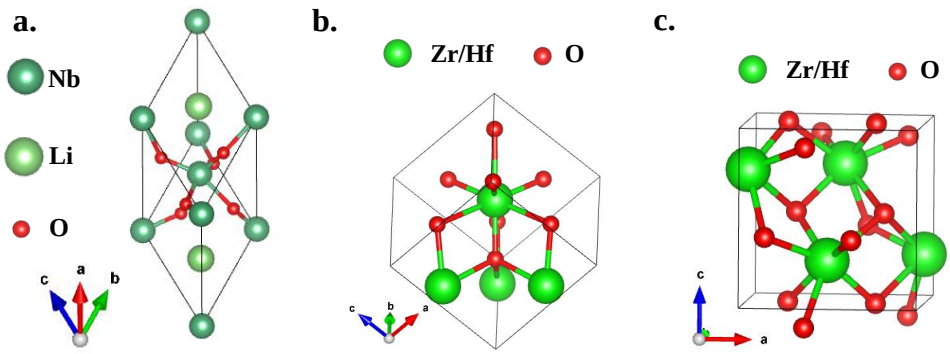

Figure 1: The crystallographic structures of a) $LiNbO_3$ (space group R3c), b) rhombohedral ZrO_2-HfO_2 (space group R3m), and c) orthorhombic ZrO_2-HfO_2 (space group $Pbc2_1$).

3.1 LNO rhombohedral R3c

We started our calculations with LNO, which features a ferroelectric R3c ground state at low temperatures. The crystal structure of the bulk system, built from ten atoms per unit cell, is shown in Figure 1a (lattice constants and atomic coordinates are given in Table S.1 in Supplemental Material

(SM) [66]). Computed band gaps, dynamic refractive indices n_{ii} and ϵ_{ii} values of LNO determined with three functionals of different types, namely B3LYP, PBE0, and PBE at an optical frequency corresponding to 633 nm wavelength, are listed in Table 1. Apart from electronic contributions, which can be trivially computed with the CPKS approach, the reported values comprise as well the respective vibrational contributions computed at the same level of theory. The wavelength (633 nm) was chosen to compare our results to available data reported in the literature; both experimental and theoretical data are reported in Table 1. Note that the EO properties are also investigated up to the near-infrared wavelength range in section 3.2.

Starting from the computed bandgap of LNO, it is seen that out of the three methods used, B3LYP and PBE0 yield notably larger values as compared to the reported experimental values. On the other hand, the pure PBE functional follows the opposite trend. The frequently cited direct band gap value of LNO, mostly concluded from optical experiments [67], is about 3.78 eV. However, this value should be considered with care due to electron-hole attraction effects, which might induce important underestimations in the final outcome of optical measurement, as already discussed in Refs. [68, 69]. Therefore, for LNO crystal, a band gap of 4.7 eV [68] should be considered more suitable for comparisons between theory and experiment. Bearing in mind the latter correction, the B3LYP functional and the associated basis set reproduce the band gap of LNO better than PBE.

Turning our attention to the refractive indices computed in this study, we also notice that both B3LYP and PBE0 functionals yield values that fall very close to the available experimental measurements. On the other hand, pure PBE overshoots the experimental reference values, yielding values close to the earlier Local-Density approximations (LDA) reported results. This behavior is not surprising since pure DFT functionals generally underestimate the gap returning overestimated cell polarizabilities α_{ij} [50] and dielectric constants. Hence, it is expected to affect the refractive indices (equation 8). Nonetheless, despite the apparent deviations in functional performance, all methods considered predict relatively stable birefringence values (denoted δn in Table 1), in good agreement with the available experimental measurements conducted on stoichiometric LNO crystals (cationic ratio Li/Nb ~ 1) [70, 71].

Table 1: Band gap, refractive indices n_{ii}, the birefringence δn, and dielectric constants ϵ_{ii} of LNO calculated at 633 nm wavelength using different functionals and compared to experimental results. Values in parentheses correspond to the static values (at "infinite" wavelength).

	B3LYP	PBE0	PBE	LDA [72]	exp [70]	exp [73]
Gap (eV)	4.75	5.29	3.15	-	3.78	-
n_{xx} (n_o)	2.257	2.227	2.497	2.37	2.28	2.286
n_{zz} (n_e)	2.149	2.120	2.402	2.35	2.18	2.202
δn	0.107	0.107	0.095	/	0.098	0.09
ϵ_{xx}	5.10 (4.71)	4.96	6.23	/	/	/
ϵ_{zz}	4.63 (4.31)	4.50	5.77	/	/	/

The clamped EO coefficients r^S_{ijk} of LNO, together with the corresponding electronic and vibrational contributions computed with the B3LYP functional, are listed in Table 2. We also list previous published experimental measurements and theoretical data in the same table. All properties have been deducted from computed $\chi^{(2)}_{ijk}(-\omega_\sigma;\omega,0)$ (for Pockels coefficient calculation, ω stands for a laser wavelength, $\omega = 0$ for a static electric field, and ω_σ is the sum of two wavelengths, see SM for more details [66]) obtained at the same level of theory, considering only the four EO independent tensorial components of LNO r_{33}, r_{13}, r_{11}, and r_{51} [72]. The vibrational contribution is a result of the transverse optical phonon modes; they can be represented as $4A_1 + 5A_2 + 9E$, where the A_1 and E modes are Raman and infrared (IR) active; in contrast, A_2 modes are silent. The A_1 modes are coupled to r_{33} and r_{13}, while the E modes are linked to r_{11} and r_{51}. The corresponding computed phonon frequencies, showing a good agreement with available experimental data, together with the second-order nonlinear susceptibilities $\chi^{(2)}_{ijk}(-\omega_\sigma;\omega,0)$ at a wavelength of 633 nm, are given in SM [66]. Looking at the computed clamped EO coefficients presented in Table 2, the results obtained with B3LYP functional are in very good agreement with experimental results, notably for r_{33} and r_{13} coefficients. On the other hand, an overestimation of r_{11} and an underestimation of r_{51}, respectively, are revealed. Nevertheless, our calculations expose that the most dominant contribution out of the two considered for r^S_{ijk} is the vibrational contribution to the microscopic second hyperpolarizability of the unit cell. This result, relying on a hybrid DFT treatment of the wavefunction, confirms previous computations within the LDA approximation [72], producing at the same time a very good estimation of the EO tensorial components with respect to the experimental data.

Table 2: $r_{ijk}(-\omega_\sigma;\omega,0)$ EO tensor (pm/V) of LNO at 633 nm wavelength: electronic and ionic (clamped), and piezoelectric (unclamped) contributions, together with results from previous calculations and experiments.

		B3LYP			LDA [72]	exp [11]	exp [74]
Clamped		r^{ele}_{ijk}	r^{vib}_{ijk}	r^S_{ijk}			
	r_{33}	7.19	23.45	30.64	26.9	30.8	34
	r_{13}	2.74	7.94	10.68	9.7	8.6	10.9
	r_{11}	-1.02	-6.84	-7.86	4.6	3.4	/
	r_{51}	3.08	19.43	22.51	14.9	28	/
Unclamped		r^p_{ijk}		r_{ijk}			exp [75]
	r_{33}	0.95		31.59	27	32.6	/
	r_{13}	1.42		12.1	10.5	10	/
	r_{11}	0.86		-7.00	7.5	6	9.9
	r_{51}	10.77		33.28	28.6	32.2	/

We now consider the total unclamped EO coefficients r_{ijk} of LNO, including the piezoelectric contribution, which is computed at the same level of theory as discussed above. We note that the

photoelastic constants $P_{ij\mu\nu}$, here computed at 633 nm, are found relatively independent on wavelength above 633 nm (see Figure S.2 in SM [66]). The same trend has been observed for MgO and $CaWO_4$ crystals from calculations at the PBE level [51, 53]. The piezoelectric contribution to the EO coefficients is listed in Table 2 as r^P_{ijk}. Looking at the total $r_{ijk} = r^S_{ijk} + r^p_{ijk}$, an excellent agreement with experimental results is obtained. For the three coefficients r_{33}, r_{13}, and r_{11}, the vibrational contribution is still dominant, while r_{51} coefficient has the highest piezoelectric contribution (Table 2). Three functionals, B3LYP (Table 2), PBE0, and PBE (Table S.5), give a piezoelectric contribution to r_{51} of around 11 pm/V, that represents around 33 % of r_{51} unclamped value, lower than the 48 % found in Ref. [72]. Nevertheless, the r_{51} EO coefficient is found with the highest piezoelectric contribution from the four independent EO coefficients of LNO material, in line with the previous theoretical results [72]. Experimentally, only a piezoelectric contribution of about 4.2 pm/V has been reported [11]. This disagreement might be due to the experimental method, which can not suppress the total piezoelectric contribution during the measurement of the clamped coefficient, as previously suggested in Ref. [72].

It is worth noting that the PBE0 functional showed an overestimation of the piezoelectric contribution to r_{33} (~6 pm/V see Table S.5), which is higher than the value obtained with B3LYP and PBE functionals (~1 pm/V close to the 1.8 pm/V found experimentally [11]). Moreover, pure PBE functional delivers a reasonable estimation of the EO coefficients (Table S.5), even though it underestimates the gap, thus, giving a high refractive index (Table 1) as discussed above. That is because underestimated gaps lead to overestimated susceptibility $\chi^{(2)}_{ijk}$; in return, this will compensate for the high values of the refractive indices when computing the EO coefficients r^S_{ijk} (see equation 5).

3.2 ZrO_2-HfO_2 orthorhombic $Pbc2_1$

In this section, we present electro-optics properties of the o−phase of ZrO_2 and HfO_2 compounds, with space group $Pbc2_1$ (No. 29). The optimization of $Pbc2_1$ ZrO_2 and HfO_2 is performed using 12 atoms in a unit cell. The optimized crystalline structure and atomic positions are given in SM [66]. The polarization was also computed for o−phase ZrO_2 and HfO_2 via Berry phase calculation using Quantum Espresso (QE) [76], in order to verify that the optimized polar phases are consistent with the ones reported in literature [20, 77]. Table 3 displays the band gap, refractive indices, and remanent polarization of o−phase ZrO_2 and HfO_2; Note that regarding optical properties, no experimental data are available for comparison. However, we did obtain polarization values similar to previous calculations [77].

It is well known that ZrO_2 and HfO_2 compounds have a wide band gap, as they are used for high-k applications. From Table 3 it can be seen that the band gap of o-HfO_2 is higher by about 1 eV compared to o-ZrO_2. Another feature is that the refractive indices at 633 nm of o-ZrO_2 are higher than the ones of o-HfO_2. This is interesting because a high refractive index is an essential element for silicon photonics applications in order to ensure a sufficient contrast with the refractive index of SiO_2 [16].

Table 3: Band gap and refractive indices of orthorhombic $Pbc2_1$ ZrO_2 and HfO_2 at 633 nm. The polarization P_b (along the b axis) from Berry phase calculation is also shown.

	o-ZrO_2	o-HfO_2
gap (eV)	5.40	6.45
n_{xx}	2.204	2.059
n_{yy}	2.301	2.122
n_{zz}	2.236	2.081
P_b (μC/cm^2)	54 (58, [77])	49.5 (50, [77])

We also have to consider the vibrational modes of the $Pbc2_1$ phase, as these modes are directly linked and contribute to the EO coefficients. The primitive unit cell of $Pbc2_1$ phase with 12 atoms (4 formula units) results in 36 vibrational modes, 3 for translation modes, and 33 optical modes, having the following irreducible representation at the zone center Γ:

$$\Gamma = 8A_1 + 9A_2 + 8B_1 + 8B_2 \tag{11}$$

The A_1, B_1, and B_2 modes are Raman and IR active. Hence, they will contribute to the electro-optic coefficients, while A_2 modes are only Raman active. The calculated A_1 phonon frequencies are given in Table 4, and the A_2, B_1, and B_2 phonon frequencies are given in SM [66]. Only a few experimental results concerning the phonon frequencies of $Pbc2_1$ o−phase are available for pure ZrO_2 and HfO_2. They are displayed for o-ZrO_2 in Table 4, showing a good agreement with the calculated phonon modes.

Table 4: Calculated frequencies (cm^{-1}) of Raman and IR active A_1 phonon modes of ferroelectric ZrO_2 and HfO_2 using B3LYP functional.

	o-ZrO_2		o-HfO_2	r-ZrO_2	r-HfO_2
		exp [78]			
A_1	102	/	113	171	118
	186	200	153	220	171
	291	/	253	267	267
	315	320	295	352	284
	351	340	329	449	423
	387	/	369	534	537
	445	/	451	674	692
	566	580	589	755	770

The orthorhombic $Pbc2_1$ with a 2mm point group has five independent EO coefficients [79]: r_{13}, r_{23}, r_{33}, r_{42}, and r_{51}. Moreover, as given above, only A_1, B_1, and B_2 contribute to the EO coefficients in the $Pbc2_1$ phase. The A_1 modes are linked to r_{13}, r_{23}, and r_{33}, the B_1 and B_2 modes are coupled to r_{42} and r_{51}, respectively. These five EO coefficients are computed at the same level of theory as discussed for LNO, and they are listed in Table 5 showing the three different contributions, electronic r^{ele}_{ijk}, vibrational r^{vib}_{ijk}, and piezoelectric r^{p}_{ijk}. The first significant result is that the EO coefficients in o-ZrO_2 are higher and almost twice the ones in o-HfO_2. The r_{13} and r_{33} coefficients have the highest values of the five independent EO elements. For both ZrO_2 and HfO_2, these two coefficients have an opposite sign and are quite close in absolute values. Comparing the calculated EO results of o-ZrO_2 to those of the reference LNO material (Table 2), the r_{13} of o-ZrO_2 is close to the r_{13} of LNO, while the r_{33} of o-ZrO_2 is around one-third of LNO. Unfortunately, no experiment results are available for pure o-ZrO_2 and o-HfO_2. However, for Y_2O_3-doped HfO_2 o−phase, EO coefficients have been reported with effective values of about 0.46 pm/V and 0.67 pm/V for (100) and (111) oriented thin films, respectively [41, 42].

From Table 5, we also deduce that ionic is the dominant contribution to the EO coefficients in o−phase ZrO_2 and HfO_2, as in LNO. The approach used here for EO calculations also provides further insights into this ionic contribution computed by evaluating the Raman and IR intensities [49], as described in refs. [47] and [45], respectively. In the case of LNO crystal, we found that the two A_1 and E polar modes of lowest frequency contribute the most to r_{33} and r_{51}, respectively, amounting to 43% and 36% of the value of these coefficients. This observation is in good agreement with previous calculations [72], and with the fact that for LNO, unstable phonon modes in the paraelectric phase transform into lower frequency and highly polar modes in the low-temperature ferroelectric phase [72]. Nevertheless, ZrO_2 and HfO_2 materials have numerous polymorphs [80] and other mechanisms that can stabilize the ferroelectric phase [77, 81], away from the classical paraelectric-ferroelectric phase transition picture. However, looking at the lowest phonon modes in o-ZrO_2, the same trend is observed as in LNO material. For example, the lowest frequency A_1 TO (transverse optical) mode at 102 cm^{-1} (Table 4) is responsible for about 40% and more than 60% of the values of r_{33} and r_{13} in o-ZrO_2, respectively.

Table 5: The five independent elements of $r_{ijk}(-\omega_\sigma;\omega,0)$ tensor for $Pbc2_1$ space group, together with their respective electronic, vibrational and piezoelectric contributions, computed at a wavelength of 633 nm. All values are given in pm/V.

	o-ZrO_2				o-HfO_2			
	r^{ele}_{ijk}	r^{vib}_{ijk}	r^{p}_{ijk}	r_{ijk}	r^{ele}_{ijk}	r^{vib}_{ijk}	r^{p}_{ijk}	r_{ijk}
r_{33}	2.10	8.75	0.5	11.35	1.52	5.56	0.14	7.22
r_{13}	-1.49	- 9.29	-1.38	-12.17	-0.81	-6.32	-0.83	-7.96
r_{23}	-0.51	-2.19	0	-2.70	-0.51	-1.94	0	-2.58
r_{42}	- 0.53	-0.95	0	-1.48	-0.54	-0.83	0	-1.37
r_{51}	-1.00	-1.16	0	-2.16	-0.83	-0.94	0	-1.77

Wavelength dependence of EO coefficients: The EO values reported above are computed at 633 nm, while, for example, wavelengths for telecom applications are in the near-infrared region, typically around 1500 nm. Therefore, with a focus on the influence of laser wavelength on Pockels coefficients, the same calculations as performed at 633 nm were repeated at different wavelengths up to near-infrared. The results are displayed in Figure 2 for the unclamped r_{33} and r_{13} coefficients of LNO and o-ZrO_2. ZrO_2 is here chosen instead of HfO_2 because of its higher EO coefficients compared to HfO_2 (Table 5).

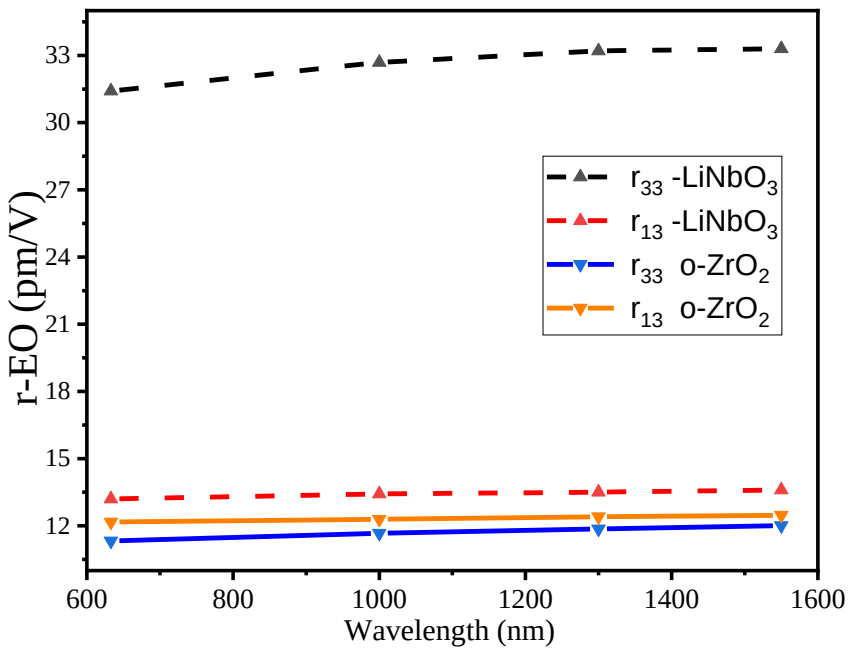

Figure 2: EO coefficients (unclamped) r_{33} and r_{13} of LNO and o-ZrO_2 at different wavelengths using B3LYP functional.

First, bearing in mind that the three contributions depend on wavelength, the electronic part is more sensitive to the electric field than the vibrational and piezoelectric contributions. Also, the electronic part depends strongly on the gap of the materials. Therefore, approaching the IR wavelengths, the electronic contribution decreases and converges to a static value [48,49]. This decrease is associated with a decrease in the refractive indices: At a wavelength of 1550 nm, the refractive index n_{zz} is found to be 2.08 (2.19) for LNO (for ZrO_2), which is lower than the value obtained at 633 nm (Tables 1 and 3). We found that the vibrational contribution remains almost constant from 633 nm to 1550 nm. The last contribution is piezoelectric, where the dependency on wavelength comes from the photoelastic coefficients, which remain relatively constant at high wavelengths (see Figure S1 in SM [66]). The general relative increase of the total EO coefficients observed in Figure 2 when increasing the wavelength is thus due to the decrease of the refractive indices (see equation 9). The EO coefficients of o-ZrO_2 are found lower than the ones of LNO at all investigated wavelengths.

Nevertheless, in terms of applications, other parameters should be taken into consideration, such as the refractive index and the total dielectric constant, to define a figure of merit (n^3 r_{ijk}/ϵ [27], with ϵ a total dielectric constant comprising both the electronic and the ionic contributions) that could bring o−phase ZrO_2/HfO_2 as a competitive material for EO applications. Figure 3 displays the comparison of this figure of merit between LNO, HfO_2 and ZrO_2 materials. For r_{33} coefficient, LNO has the highest figure of merit; however, the ones for ZrO_2 and HfO_2 are not negligible. Considering the compatibility of ZrO_2 and HfO_2 with silicon, these results are significant enough for further investigating different paths to increase the EO coefficients in these materials.

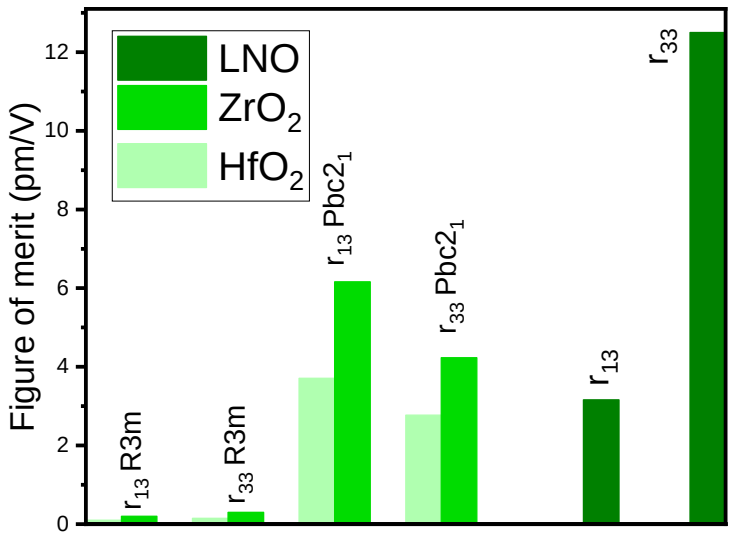

Figure 3: Figure of merit (n^3 r_{ijk}/ϵ) of HfO_2 and ZrO_2 compared to LNO using r_{33} and r_{13} coefficients.

3.3 ZrO_2-HfO_2 rhombohedral R3m

In this section, we focus on the EO properties of the rhombohedral R3m (space group No. 160) phase of ZrO_2-HfO_2. This phase is less studied than the orthorhombic phase and has only been reported in compressively strained epitaxial thin films [21, 36]. For the EO investigation, we also used a unit cell of 12 atoms (4 formula units). One should note that in the case of the r−phase, an instability (with negative/imaginary frequency) of TO A_1-TO_1 phonon mode was observed when the phonon was computed at the optimized unit cell volume for r-ZrO_2 (141 Å^3) and r-HfO_2 (136 Å^3), the optimized unit cells being given in SM [66]. For the calculation of EO coefficients and other properties to be reliable, one should have only real frequencies. To achieve such a condition for ZrO_2, an experimental volume (~132 Å^3) was imposed together with a rhombohedral angle equal to 89.56° [36], forcing the imaginary phonon mode that is calculated at $82i\ cm^{-1}$ to move to 76 cm^{-1} at the experimental volume. While for HfO_2, no r−phase unit cell volume was experimentally

reported, the volume was reduced until achieving a positive phonon frequency, and the volume used here is 128 Å^3.

Table 6: Band gap and refractive indices of rhombohedral R3m ZrO_2 and HfO_2 at 633 nm. The rhombohedral polarization P_r from Berry phase calculation is also shown.

	r-ZrO_2	r-HfO_2
gap (eV)	5.79	6.77
n_{xx}	2.282	2.114
n_{zz}	2.271	2.107
δn	0.011	0.007
P_r (μC/cm^2)	6.8	5.1

The computed band gap, refractive indices, and polarization are displayed in Table 6. The band gaps obtained for ZrO_2 and HfO_2 in the r−phase are significantly higher than in the o−phase. The remanent polarization for the r−phase was also computed via Berry Phase using QE. The value obtained for the polarization is lower than in the case of the o−phase, as expected from previous calculations [21, 35]. Note that this polarization depends strongly on the compressive strain, which is directly related to the rhombohedral angle [21, 36]. Here, the polarization is computed at a fixed angle using the rhombohedral primitive unit cell. In contrast, in Refs. [21, 35] the polarization is computed with hexagonal unit cells and at different compressive strains.

Table 7: The four independent elements of $r_{ijk}(-\omega_\sigma;\omega,0)$ tensor for R3m space group, together with their respective electronic, vibrational and piezoelectric contributions, computed at a wavelength of 633 nm. All values are given in pm/V.

	r-ZrO_2				r-HfO_2			
	r^{ele}_{ijk}	r^{vib}_{ijk}	r^{p}_{ijk}	r_{ijk}	r^{ele}_{ijk}	r^{vib}_{ijk}	r^{p}_{ijk}	r_{ijk}
r_{33}	- 0.11	- 0.30	-0.01	-0.42	-0.07	-0.21	-0.02	-0.30
r_{13}	0.05	0.14	0.05	0.24	0.03	0.13	0.11	0.27
r_{11}	-0.06	-0.21	-0.20	-0.28	-0.05	-0.08	-0.16	0.29
r_{51}	0.05	0.08	-0.25	-0.12	0.03	0.21	-0.19	0.05

As seen for o−phase (section 3.2), a unit cell with 12 atoms results in 36 vibrational modes, 3 for translation modes, and 33 for optical phonon modes. In the case of R3m space group, there are three different modes A_1, A_2, and E; the irreducible representation at Γ zone center is:

$$\Gamma = 8A_1 + 3A_2 + 11E \tag{12}$$

The A_1 and (degenerate) E modes are simultaneously Raman and IR active, while the A_2 modes are Raman active and IR inactive. The calculated A_1 mode frequencies are shown in Table 4 for ZrO_2 and HfO_2, experimentally no data are available for ZrO_2-HfO_2 in r−phase. The E and A_2 phonon frequencies are given in SM (Table S.8 in SM [66])
Following the same method as described in sections 3.1 and 3.2, the EO coefficients obtained for ZrO_2 and HfO_2 r−phase are given in Table 7. Comparing these EO coefficients to the ones of LNO and o−phase, r−phase shows very modest EO values. This trend is also observed in terms of remanent polarization obtained for r−phase compared to orthorhombic $Pbc2_1$ (Tables 3 and 6).

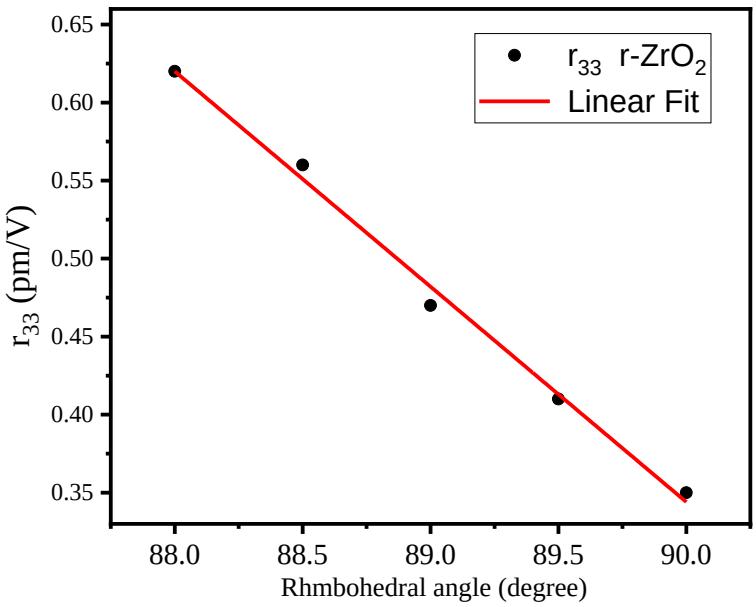

Figure 4: r_{33} EO coefficient of r- ZrO_2 computed at different angles.

Strain dependence of EO coefficients: Because the ZrO_2-HfO_2 R3m phase has a strong dependence on the compressive strain, r_{33} EO coefficient of r-ZrO_2 is computed at different rhombohedral angles. The results are displayed in Figure 4, showing a linear dependence of r_{33} with respect to the rhombohedral angle. Even at a high compressive strain (rhombohedral angle of 88°), the EO coefficient is still lower than the one calculated for o-ZrO_2. Two main reasons cause the low EO coefficients of r-ZrO_2 compared to o-ZrO_2. First is the relatively high band gap in the r−phase, which reduces the electronic contribution. The second reason is that the A_1 low-frequency phonon modes have negligible contributions to EO coefficients in the r−phase, while similar modes highly contribute to the ones of the o−phase (see section 3.2). In more details, for the r−phase, from 8 A_1 active modes (Table 4), only 3 modes at 220, 352, and 449 cm^{-1} contribute significantly to r_{33} and r_{13}. The modes at 220 and 352 cm^{-1} give almost the same value of the hyper-polarizabilities β_{33} (equation 6), but with opposite signs, hence they cancel each other, therefore solely the mode at

449 cm^{-1} is contributing to r_{33}. This is the most probable reason why the r−phase shows a lower EO coefficient than the o−phase. Finally, this gives r−phase a very low figure of merit compared to o−phase and to LNO as illustrated in Figure 3.

4 Conclusion

In conclusion, we investigated the electro-optic Pockels coefficients of the ZrO_2 and HfO_2 compounds in two noncentrosymmetric phases: rhombohedral R3m and orthorhombic $Pbc2_1$. We determined that the o−phase has considerably higher EO coefficients than the r−phase. This remains true for a highly strained rhombohedral phase; the optical nonlinearity is weak compared to the o−phase. Moreover, r_{33} and r_{13} in the orthorhombic phase are higher in ZrO_2 than in HfO_2, with values of about 12 and 7 pm/V for ZrO_2 and HfO_2, respectively. Comparing the EO coefficients of o-ZrO_2 to rhombohedral $LiNbO_3$ reference material, the r_{13} coefficient shows a comparable value to the r_{13} of $LiNbO_3$. In contrast, the r_{33} coefficient of o-ZrO_2 is three times lower than the r_{33} of $LiNbO_3$. We observed that the polar and low-frequency phonon modes contribute most to the EO in the orthorhombic phase; the same trend is also observed in $LiNbO_3$. Our numerical results suggest that the ferroelectric orthorhombic phase of ZrO_2 and HfO_2-based thin films can be relevant for EO applications when considering their compatibility with silicon. Finally, considering the dominant contribution by the ionic part as identified in this work, we believe that doping ZrO_2/HfO_2 with a suitable element to stabilize the orthorhombic phase but also increase the ionicity of these materials will lead to high EO coefficients. Thus, ZrO_2/HfO_2-based compounds may be promising candidates for EO properties and their use in photonic devices.

Acknowledgements: This work has received support from the Agence nationale de la recherche (ANR) under project FOIST (N°ANR-18-CE24-0030), and from the French national network RENATECH for nanofabrication.

SUPPLEMENTAL MATERIAL

EO coefficients of $LiNbO_3$ and ZrO_2-HfO_2 materials

The electro-optic (EO) coefficients for 3m space group (SG) [79], thus for ZrO_2-HfO_2 rhombohedral R3m (SG N° 160) and $LiNbO_3$ R3c (SG N° 161), have 4 independent EO coefficients with two possible representation:

$$m \perp x_1 \begin{vmatrix} r_{11} & 0 & r_{13} \\ -r_{11} & 0 & r_{13} \\ 0 & 0 & r_{33} \\ 0 & r_{51} & 0 \\ r_{51} & 0 & 0 \\ 0 & -r_{11} & 0 \end{vmatrix} \qquad or \qquad m \perp x_2 \begin{vmatrix} 0 & -r_{22} & r_{13} \\ 0 & r_{22} & r_{13} \\ 0 & 0 & r_{33} \\ 0 & r_{51} & 0 \\ r_{51} & 0 & 0 \\ -r_{22} & 0 & 0 \end{vmatrix} \tag{1}$$

In the case of $Pbc2_1$ (SG N° 29 and 2mm point group), there are five independent electro-optic coefficients:

$$\begin{vmatrix} 0 & 0 & r_{13} \\ 0 & 0 & r_{23} \\ 0 & 0 & r_{33} \\ 0 & r_{42} & 0 \\ r_{51} & 0 & 0 \\ 0 & 0 & 0 \end{vmatrix} \tag{2}$$

Symmetry of β (SHG) and β (EO / dc-Pockels)

In the general case, the second order non-linearity β_{ijk} is written as

$$\beta_{ijk} = \beta_{ijk}(-\omega_\sigma;\omega_1,\omega_2) \tag{3}$$

Second harmonic generation (SHG)
For SHG, β_{ijk} ($\omega_\sigma = 2\,\omega$ and $\omega_1 = \omega_2 = \omega$) can be written as

$$\beta_{ijk} = \beta_{ijk}(-2\omega;\omega,\omega) \tag{4}$$

So in the case of second harmonic generation, for example with β_{yxy} equal to β_{yyx}, in general the symmetry given in (4) can simply be written as $\beta_{ijk}(-2\omega;\omega,\omega) = \beta_{ikj}(-2\omega;\omega,\omega)$.

EO / dc-Pockels effect
For dc-Pockels effect, β_{ijk} ($\omega_\sigma = \omega$, $\omega_1 = \omega$, and $\omega_2 = 0$) is written as

$$\beta_{ijk} = \beta_{ijk}(-\omega;\omega,0) = \beta_{ikj}(-\omega;0,\omega) \tag{5}$$

The same permutation as given above for SHG then leads to β_{xxz} (-ω; ω,0) = β_{xzx}(-ω; 0, ω). In other words, β_{xxz} (-ω; ω,0) tensor element, where the static field is along z, is equal to β_{xzx}(-ω; 0, ω), so that the static electric field is always applied along z direction. But β_{xxz} (-ω; ω,0) is not equal to β_{xzx} (-ω; ω, 0) because in the latter tensor element the static electric field is along x. Finally, this will ensure that r_{ijk} coefficients respect the permutation $r_{ijk} = r_{jik}$.

Results

$LiNbO_3$

$LiNbO_3$	a (Å)	b (Å)	c (Å)
	5.216	5.216	14.14
Atom	x/a	y/b	z/c
Li	0	0	0.2614
Nb	0	0	-0.0188
O	-0.0473	0.3435	0.0441
V (Å^3)	111		

Table 1: The optimized geometry for $LiNbO_3$, on the right the $LiNbO_3$ R3c structure.

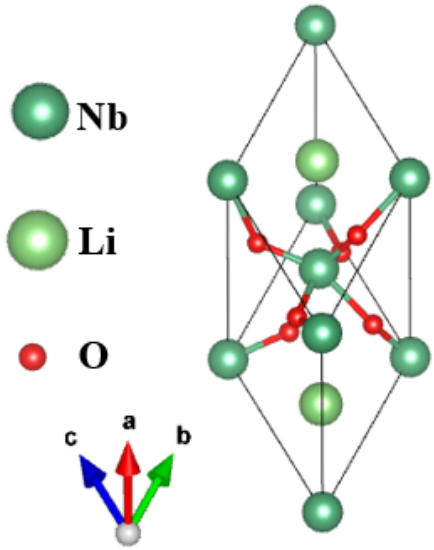

The refractive indices of LiNbO3 calculated using B3LYP functional, together with the electronic and vibrational contributions to the polarizability α_{ij}, are reported in Table 2. The ionic contribution at 633 nm is almost null.

Table 2: Refractive indices n_{ii} of $LiNbO_3$ at 633 nm wavelength using B3LYP functional, showing the electronic and vibrational contributions to the polarizability α_{ij}.

	electronic	vibrational	n_{ii}
α_{xx}	244.77	-0.60	2.257
α_{yy}	244.77	-0.60	2.257
α_{zz}	216.36	-0.48	2.149

At the Γ point, the optical phonons of $LiNbO_3$ can be classified according to the irreducible representation of the space group R3c into $\Gamma = 4A_1 + 5A_2 + 9E$. The A_1 and E modes are Raman and infrared active, while A_2 modes are inactive.

The calculated frequencies of the A_1 and E modes are shown in Table 3 and compared with previous theoretical and experimental data. There is a good agreement between our calculations and available experimental values. In particular, B3LYP functional calculated frequencies are close to the experimental ones, with only a relative underestimate of the first A_1 mode. This might be due to the anharmonicity of this mode: The experimental frequency is substantially higher than the one calculated in the harmonic approximation; Considering the one-dimensional non-interacting oscillator approximation, a good approximation to the experimental value was obtained by Inbar and Cohen [82]. Increasing HF exchange (PBE0) gives relatively higher frequency values, while decreasing exchange (PBE(10%) and PBE) brings lower values compared to the experimental results.

Table 3: Raman and IR active phonon mode frequencies (cm^{-1}) of ferroelectric $LiNbO_3$ calculated with several functionals, compared with previous theoretical and experimental results.

	B3LYB	PBE0	PBE(10%)	PBE	LDA [83]	exp [84]	exp [85]
A1	232	251	242	234	208	256	/
	275	291	279	271	279	275	/
	340	346	332	322	344	332	/
	636	650	628	611	583	637	/
E	143	152	144	140	151	/	155
	233	241	229	221	/	/	238
	246	259	250	245	236	/	265
	304	315	302	294	307	/	325
	344	367	252	343	334	/	/
	361	380	365	355	352	/	/
	427	434	414	402	432	/	431
	576	589	572	560	526	/	582
	655	674	654	641	617	/	668

In order to obtain the EO coefficients of $LiNbO_3$ using CRYSTAL17, we computed the electronic and vibrational contributions to the second hyperpolarizability $\beta_{ijk}(-\omega_\sigma;\omega,0)$ at a wavelength of 633 nm as described in the main paper, then deduced the $\chi^{(2)}_{ijk}(-\omega_\sigma;\omega,0)$ values that are given in Table 4 (see the main paper for the relation between the susceptibility $\chi^{(2)}_{ijk}$ and the hyperpolarizability β_{ijk}). For symmetry reasons, only 11 out of 27 elements of the rank three $\chi^{(2)}_{ijk}$ tensor are not null and only four elements are independent. These four elements are given in Table 4. We note that pure PBE functional gives the highest values of $\chi^{(2)}_{ijk}$, that is because pure DFT-PBE underestimates the gap, as discussed in the main paper.

Table 4: Non-zero elements of $\chi^{(2)}_{ijk}(-\omega_\sigma;\omega,0)$ (pm/V) tensor in $LiNbO_3$ computed at a wavelength of 633 nm using different functionals, with their vibrational and electronic contributions.

	B3LYP		PBE0		PBE(10%)		PBE	
$\chi^{(2)}_{ijk}$	vib	ele	vib	ele	vib	ele	vib	ele
xxx	88.83	13.28	66.43	8.18	104.8	19.53	136.17	50.30
xxz	-103.00	-35.50	-84.37	-28	-129.2	-53.15	-183.4	-66.36
yzy	-228.52	-36.56	-188.73	-27.60	-269.1	-54.53	-338.5	-102.4
zzz	-250.08	-76.66	-220.04	-63.05	-296.9	-103.1	-396.05	-117.8

Table 5 gives the clamped and unclamped EO coefficients of $LiNbO_3$, considering only the four independent elements of r_{ijk}, and compares them with previous calculations and experiments. All functionals used in the present study agree well with experimental results, notably for the r_{33} and r_{13} coefficients. The clamped EO coefficients, taking in consideration the piezoelectric contribution, are also given in Table 4.

Table 5: Total $r_{ijk}(-\omega_\sigma;\omega,0)$ EO tensor (pm/V) in $LiNbO_3$ computed at a wavelength of 633 nm using different functionals, together with previous calculations and experiments.

		B3LYB	PBE0	PBE(10%)	PBE	LDA [72]	exp [11]	exp [74]
clamped	r_{33}	30.64	28.02	30.45	30.87	26.9	30.8	34
	r_{13}	10.68	9.14	11.39	12.84	9.7	8.6	10.9
	r_{11}	-7.86	-6.06	-7.79	-9.59	4.6	3.4	/
	r_{51}	22.51	19.41	21.99	24.51	14.9	28	/
unclamped								exp [75]
	r_{33}	31.59	34.32	30.90	31.20	27	32.6	/
	r_{13}	12.10	10.92	12.61	13.81	10.5	10	/
	r_{11}	-7.00	-5.00	-6.84	-10.20	7.5	6	9.9
	r_{51}	33.28	27.09	31.94	34.04	28.6	32.2	/

As the experimental values of EO coefficients are usually measured at finite electric field wavelength, in Figure 1 we show the dependence of photoelastic coefficients on the electric field wavelength (nm). From 633 nm up to the near-infrared wavelength range, the two coefficients remain almost constant, while below 633 nm a decrease is observed.

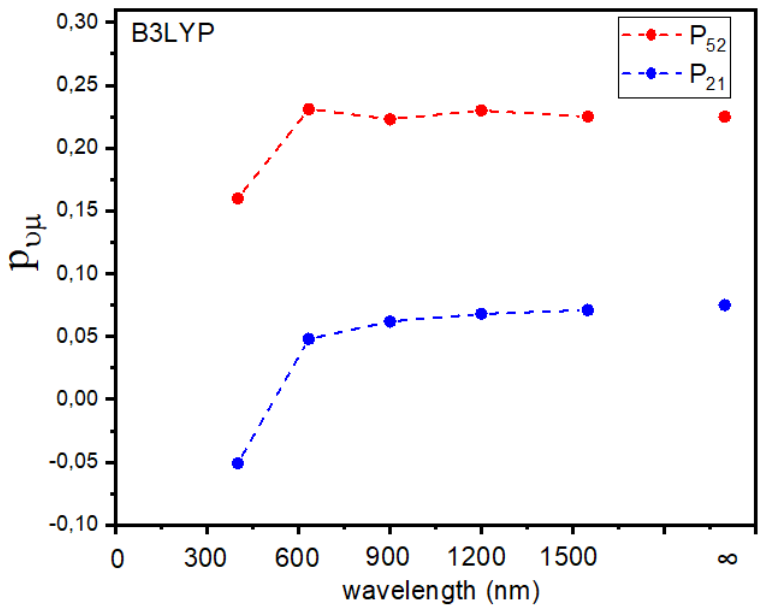

Figure 1: Independent photoelastic p_{52} and p_{21} coefficients of the $LiNbO_3$ crystal computed at B3LYP level as a function of the electric field wavelength (nm).

ZrO_2-HfO_2

Table 6: The optimized geometry for ZrO_2 orthorhombic $Pbc2_1$.

o-ZrO_2	a (Å)	b (Å)	c (Å)
	5.34	5.14	5.16
Atom	x/a	y/b	z/c
Zr	0.0274	0.2644	-0.2545
O1	0.3602	0.0619	-0.1021
O2	0.2262	-0.4688	-0.0064
V ($Å^3$)	141.62		

Table 7: The optimized geometry for HfO_2 orthorhombic $Pbc2_1$.

o-ZrO_2	a (Å)	b (Å)	c (Å)
	5.28	5.07	5.10
Atom	x/a	y/b	z/c
Zr	0.0312	0.2651	-0.2551
O1	0.3618	0.0638	-0.1051
O2	0.2267	-0.4699	-0.00278
V ($Å^3$)	136.52		

The orthorhombic $Pbc2_1$ phase with a unit of 12 atoms (4 formula units) results in 36 vibrational modes, 3 for translation modes, and 33 optical phonon modes having the following irreducible representation at the zone center Γ:

$$\Gamma = 8A_1 + 9A_2 + 8B_1 + 8B_2$$

The computed phonon frequencies are listed in Table 1 .

For the rhombohedral phase R3m, also with a unit of 12 atoms (4 formula units) resulting in 36 vibrational modes, 3 for translation modes and 33 optical phonon modes, the irreducible representation at the zone center Γ is:

$$\Gamma = 8A_1 + 3A_2 + 11E$$

The calculated frequencies are given in Table 1. Note that the computed E modes here are degenerate. The lowest E-TO1 (transverse optical) mode frequency depends strongly on the unit cell volume and can also be affected by other factors, like strain, oxygen vacancies, etc.

Table 8: Raman and IR phonon mode frequencies (cm^{-1}) of ferroelectric ZrO_2 and HfO_2 calculated using B3LYP functional. Experimental data are also reported when available.

	o-ZrO_2		o-HfO_2		r-ZrO_2	r-HfO_2
	B3LYP	exp [78]	B3LYP		B3LYP	B3LYP
A_1	102	/	113	A_1	171	118
	186	200	153		220	171
	291	/	253		267	267
	315	320	295		352	284
	351	340	329		449	423
	387	/	369		534	537
	445	/	451		674	692
	566	580	589		755	770
A_2	172	/	122	A_2	169	117
	180	/	134		332	312
	192	200	148		586	595
	295	/	303			
	400	/	414	E	76	20
	482	/	496		165	114
	561	/	581		174	123
	634	/	654		233	187
	659	/	674		325	271
B_1	188	/	141		358	304
	224	/	218		456	436
	298	/	238		536	540
	329	/	311		586	594
	402	/	395		683	702
	514	/	533		721	726
	545	550	554			
	726	/	736			
B_2	165	/	121			
	233	/	226			
	289	/	269			
	345	/	312			
	399	/	369			
	461	/	484			
	622	620	637			
	683	/	697			

References

[1] A. K. Mohapatra, M. G. Bason, B. Butscher, K. J. Weatherill, and C. S. Adams. A giant electro-optic effect using polarizable dark states. Nature Physics, 4(11):890–894, 2008.

[2] A. Melikyan, L. Alloatti, A. Muslija, D. Hillerkuss, P. C. Schindler, J. Li, R. Palmer, D. Korn, S. Muehlbrandt, D. Van Thourhout, B. Chen, R. Dinu, M. Sommer, C. Koos, M. Kohl, W. Freude, and J. Leuthold. High-speed plasmonic phase modulators. Nature Photonics, 8(3):229–233, 2014.

[3] A. Rueda, F. Sedlmeir, M. Kumari, G. Leuchs, and H. G. L. Schwefel. Resonant electro-optic frequency comb. Nature, 568(7752):378–381, 2019.

[4] S. Abel, F. Eltes, J. E. Ortmann, A. Messner, P. Castera, T. Wagner, D. Urbonas, A. Rosa, A. M. Gutierrez, D. Tulli, P. Ma, B. Baeuerle, A. Josten, W. Heni, D. Caimi, L. Czornomaz, A. A. Demkov, J. Leuthold, P. Sanchis, and J. Fompeyrine. Large Pockels effect in micro- and nanostructured barium titanate integrated on silicon. Nature Materials, 18(1):42–47, 2019.

[5] J. L O'Brien, A. Furusawa, and J. Vučković. Photonic quantum technologies. Nature Photonics, 3(12):687–695, 2009.

[6] J. Wang, F. Sciarrino, A. Laing, and M. G. Thompson. Integrated photonic quantum technologies. Nature Photonics, 14(5):273–284, 2020.

[7] J. K. George, A. Mehrabian, R. Amin, J. Meng, T. F. de Lima, A. N. Tait, B. J. Shastri, T. El-Ghazawi, P. R. Prucnal, and V. J. J. Sorger. Neuromorphic photonics with electro-absorption modulators. Opt. Express, 27(4):5181–5191, Feb 2019.

[8] Y. Shen, N. C. Harris, S. Skirlo, M. Prabhu, T. Baehr-Jones, M. Hochberg, X. Sun, S. Zhao, H. Larochelle, D. Englund, and M. Soljačić. Deep learning with coherent nanophotonic circuits. Nature Photonics, 11(7):441–446, 2017.

[9] B. J. Offrein, J. Geler-Kremer, J. Weiss, R. Dangel, P. Stark, A. Sharma, S. Abel, and F. Horst. Prospects for photonic implementations of neuromorphic devices and systems. In 2020 IEEE International Electron Devices Meeting (IEDM), pages 7.4.1–7.4.4, 2020.

[10] M. E. Lines and A. M. Glass. Principles and Applications of Ferroelectrics and Related Materials. Oxford University Press, Oxford, 2001.

[11] E. H. Turner. High-frequency electro-optic coefficients of lithium niobate. 303(November 2004):303–305, 1966.

[12] E. L. Wooten, K. M. Kissa, A. Yi-Yan, E. J. Murphy, D. A. Lafaw, P. F. Hallemeier, D. Maack, D. V. Attanasio, D. J. Fritz, G. J. McBrien, and D. E. Bossi. A review of lithium niobate modulators for fiber-optic communications systems. IEEE Journal of Selected Topics in Quantum Electronics, 6(1):69–82, 2000.

[13] C. Wang, M. Zhang, X. Chen, M. Bertrand, A. Shams-Ansari, S. Chandrasekhar, P. Winzer, and M. Loncar. Integrated lithium niobate electro-optic modulators operating at CMOS-compatible voltages. Nature, 562(7725):101–104, 2018.

[14] Payam R., Jichi M., Saeed K., Jeff C., and Sasan F. Heterogeneous lithium niobate photonics on silicon substrates. Optics express, 21 21:25573–81, 2013.

[15] M. Zgonik, P. Bernasconi, M. Duelli, R. Schlesser, P. Gunter, M. H. Garrett, D. Rytz, Y. Zhu, and X. Wu. Dielectric, elastic, piezoelectric, electro-optic, and elasto-optic tensors of $BaTiO_3$ crystals. Phys. Rev. B, 50:5941–5949, Sep 1994.

[16] A. Messner, F. Eltes, P. Ma, S. Abel, B. Baeuerle, A. Josten, W. Heni, D. Caimi, J. Fompeyrine, and J. Leuthold. Plasmonic Ferroelectric Modulators. Journal of Lightwave Technology, 37(2):281–290, 2019.

[17] C. Xiong, W. H. P. Pernice, J. H. Ngai, J. W. Reiner, D. Kumah, F. J. Walker, C. H. Ahn, and H. X. Tang. Active Silicon Integrated Nanophotonics: Ferroelectric $BaTiO_3$ Devices. Nano Letters, 14(3):1419–1425, mar 2014.

[18] T. Paoletta and A. A. Demkov. Pockels effect in low-temperature rhombohedral $BaTiO_3$. Phys. Rev. B, 103:014303, Jan 2021.

[19] F. Eltes, G. E. Villarreal-Garcia, D. Caimi, H. Siegwart, A. A. Gentile, A. Hart, P. Stark, G. D. Marshall, M. G. Thompson, J. Barreto, J. Fompeyrine, and S. Abel. An integrated optical modulator operating at cryogenic temperatures. Nature Materials, 19(11):1164–1168, 2020.

[20] T. S. Böscke, J. Müller, D. Bräuhaus, U. Schröder, and U. Böttger. Ferroelectricity in hafnium oxide thin films. Applied Physics Letters, 99(10):102903, 2011.

[21] Y. Wei, P. Nukala, M. Salverda, S. Matzen, H. J. Zhao, J. Momand, A. S. Everhardt, G. Agnus, G. R. Blake, P. Lecoeur, B. J. Kooi, J. Íñiguez, B. Dkhil, and B Noheda. A rhombohedral ferroelectric phase in epitaxially strained $Hf_{0.5}Zr_{0.5}O_2$ thin films. Nature Materials, 17(12):1095–1100, 2018.

[22] T. Ali, P. Polakowski, S. Riedel, T. Büttner, T. Kämpfe, M. Rudolph, B. Pätzold, K. Seidel, D. Löhr, R. Hoffmann, M. Czernohorsky, K. Kühnel, P. Steinke, J. Calvo, K. Zimmermann, and J. Müller. High Endurance Ferroelectric Hafnium Oxide-Based FeFET Memory Without Retention Penalty. IEEE Transactions on Electron Devices, 65(9):3769–3774, 2018.

[23] J. Müller, T. S. Böscke, D. Bräuhaus, U. Schröder, U. Böttger, J. Sundqvist, P. Kücher, T. Mikolajick, and L. Frey. Ferroelectric $Zr_{0.5}Hf_{0.5}O_2$ thin films for nonvolatile memory applications. Applied Physics Letters, 99(11):112901, 2011.

[24] M. H. Park, H. J. Kim, Y. J. Kim, T. Moon, K. Do. Kim, and C. S. Hwang. Thin $Hf_xZr_{1-x}O_2$ Films: A New Lead-Free System for Electrostatic Supercapacitors with Large Energy Storage Density and Robust Thermal Stability. Advanced Energy Materials, 4(16):1400610, 2014.

[25] J. P. B. Silva, K. C. Sekhar, H. Pan, J. L. MacManus-Driscoll, and M. Pereira. Advances in dielectric thin films for energy storage applications, revealing the promise of group iv binary oxides. ACS Energy Letters, 6(6):2208–2217, 2021.

[26] D. K. Fork, F. Armani-Leplingard, and J. J. Kingston. Optical losses in ferroelectric oxide thin films: Is there light at the end of the tunnel? MRS Proceedings, 361:155, 1994.

[27] D. Sando, Y. Yang, C. Paillard, B. Dkhil, L. Bellaiche, and V. Nagarajan. Epitaxial ferroelectric oxide thin films for optical applications. Applied Physics Reviews, 5(4):041108, 2018.

[28] Suraj S Cheema, Daewoong Kwon, Nirmaan Shanker, Roberto Dos Reis, Shang-Lin Hsu, Jun Xiao, Haigang Zhang, Ryan Wagner, Adhiraj Datar, Margaret R McCarter, Claudy R Serrao, Ajay K Yadav, Golnaz Karbasian, Cheng-Hsiang Hsu, Ava J Tan, Li-Chen Wang, Vishal Thakare, Xiang Zhang, Apurva Mehta, Evguenia Karapetrova, Rajesh V Chopdekar, Padraic Shafer, Elke Arenholz, Chenming Hu, Roger Proksch, Ramamoorthy Ramesh, Jim Ciston, and Sayeef Salahuddin. Enhanced ferroelectricity in ultrathin films grown directly on silicon. Nature, 580(7804):478–482, 2020.

[29] P. Polakowski and J. Müller. Ferroelectricity in undoped hafnium oxide. Applied Physics Letters, 106(23):232905, 2015.

[30] S. Starschich, T. Schenk, U. Schroeder, and U. Boettger. Ferroelectric and piezoelectric properties of $Hf_{1-x}Zr_xO_2$ and pure ZrO_2 films. Applied Physics Letters, 110(18):182905, 2017.

[31] R. Shimura, T. Mimura, A. Tateyama, T. Shimizu, T. Yamada, Y. Tanaka, Y. Inoue, and H. Funakubo. Preparation of 1 μm thick Y−doped HfO_2 ferroelectric films on (111) $Pt/TiO_x/SiO_2/(001)Si$ substrates by a sputtering method and their ferroelectric and piezoelectric properties. Japanese Journal of Applied Physics, 60(3):031009, mar 2021.

[32] J. Lyu, I. Fina, R. Solanas, J. Fontcuberta, and F. Sánchez. Robust ferroelectricity in epitaxial $Hf_{1/2}Zr_{1/2}O_2$ thin films. Applied Physics Letters.

[33] Peijie Jiao, Jiayi Li, Zhongnan Xi, Xiaoyu Zhang, Jian Wang, Yurong Yang, Yu Deng, and Di Wu. Ferroelectric $Hf_{0.5}Zr_{0.5}O_2$ thin films deposited epitaxially on (110)−oriented $SrTiO_3$. Applied Physics Letters, 119(25):252901, 2021.

[34] Y. Yun, P. Buragohain, M. Li, Z. Ahmadi, Y. Zhang, X. Li, H. Wang, J. Li, P. Lu, L. Tao, H. Wang, J. E. Shield, E. Y. Tsymbal, A. Gruverman, and X. Xu. Intrinsic ferroelectricity in Y-doped HfO_2 thin films. Nature Materials, 21(8):903–909, 2022.

[35] J. P. B. Silva, R. F. Negrea, M. C. Istrate, S. Dutta, H. Aramberri, J. Iniguez, F. G. Figueiras, C. Ghica, K. C. Sekhar, and A. L Kholkin. Wake-up Free Ferroelectric Rhombohedral Phase in Epitaxially Strained ZrO_2 Thin Films. ACS Applied Materials and Interfaces, 13(43):51383–51392, nov 2021.

[36] A. El Boutaybi, T. Maroutian, L. Largeau, S. Matzen, and P. Lecoeur. Stabilization of the epitaxial rhombohedral ferroelectric phase in ZrO_2 by surface energy. Phys. Rev. Materials, 6:074406, Jul 2022.

[37] M. Hoffmann, M. Pešić, K. Chatterjee, Asif I. Khan, S. Salahuddin, S. Slesazeck, U. Schroeder, and T. Mikolajick. Direct Observation of Negative Capacitance in Polycrystalline Ferroelectric HfO_2. Advanced Functional Materials, 26(47):8643–8649, 2016.

[38] M. Hoffmann, S. Slesazeck, T. Mikolajick, and C. S. Hwang. Negative capacitance in hfo2- and zro2-based ferroelectrics. In Uwe Schroeder, Cheol Seong Hwang, and Hiroshi Funakubo, editors, Ferroelectricity in Doped Hafnium Oxide: Materials, Properties and Devices, Woodhead Publishing Series in Electronic and Optical Materials, pages 473–493. Woodhead Publishing, 2019.

[39] Y. Wei, S. Matzen, T. Maroutian, G. Agnus, M. Salverda, P. Nukala, Q. Chen, J. Ye, P. Lecoeur, and B. Noheda. Magnetic Tunnel Junctions Based on Ferroelectric $Hf_{0.5}Zr_{0.5}O_2$ Tunnel Barriers. Phys. Rev. Applied, 12:031001, Sep 2019.

[40] Y. Goh and S. Jeon. The effect of the bottom electrode on ferroelectric tunnel junctions based on CMOS−compatible HfO_2 . Nanotechnology, 29(33):335201, jun 2018.

[41] S. Kondo, R. Shimura, T. Teranishi, A. Kishimoto, T. Nagasaki, H. Funakubo, and T. Yamada. Linear electro-optic effect in ferroelectric HfO_2 −based epitaxial thin films. Japanese Journal of Applied Physics, 60(7):070905, jun 2021.

[42] S. Kondo, R. Shimura, T. Teranishi, A. Kishimoto, T. Nagasaki, H. Funakubo, and T. Yamada. Influence of orientation on the electro-optic effect in epitaxial Y-doped HfO_2 ferroelectric thin films. Japanese Journal of Applied Physics, 60(SF):SFFB13, aug 2021.

[43] R. Dovesi, R. Orlando, A. Erba, C. M. Zicovich-Wilson, B. Civalleri, S. Casassa, L. Maschio, M. Ferrabone, M. De La Pierre, P. D'Arco, Y. Noël, M. Causà, M. Rérat, and B. Kirtman. CRYSTAL14: A program for the ab initio investigation of crystalline solids. International Journal of Quantum Chemistry, 114(19):1287–1317, 2014.

[44] R. Dovesi, A. Erba, R. Orlando, C. M. Zicovich-Wilson, B. Civalleri, L. Maschio, M. Rérat, S. Casassa, J. Baima, S. Salustro, and B. Kirtman. Quantum-mechanical condensed matter simulations with CRYSTAL. WIREs Computational Molecular Science, 8(4):e1360, 2018.

[45] L. Maschio, B. Kirtman, M. Rérat, R. Orlando, and R. Dovesi. Ab initio analytical Raman intensities for periodic systems through a coupled perturbed Hartree-Fock/Kohn-Sham method in an atomic orbital basis. I. Theory. The Journal of Chemical Physics, 139(16):164101, 2013.

[46] L. Maschio, B. Kirtman, R. Orlando, and M. Rérat. Ab initio analytical infrared intensities for periodic systems through a coupled perturbed Hartree-Fock/Kohn-Sham method. The Journal of Chemical Physics, 137(20):204113, 2012.

[47] L. Maschio, B. Kirtman, M. Rérat, R. Orlando, and R. Dovesi. Comment on "Ab initio analytical infrared intensities for periodic systems through a coupled perturbed Hartree-Fock/Kohn-Sham method" [J. Chem. Phys. 137, 204113 (2012)]. The Journal of Chemical Physics, 139(16):167101, 2013.

[48] L. Maschio, M. Rérat, B. Kirtman, and R. Dovesi. Calculation of the dynamic first electronic hyperpolarizability $\beta(-\omega_\sigma; \omega_1, \omega_2)$ of periodic systems. Theory, validation, and application to multi-layer MoS_2. The Journal of Chemical Physics, 143(24):244102, 2015.

[49] M. Rérat, L. Maschio, B. Kirtman, B. Civalleri, and R. Dovesi. Computation of Second Harmonic Generation for Crystalline Urea and KDP. An ab Initio Approach through the Coupled Perturbed Hartree–Fock/Kohn–Sham Scheme. Journal of Chemical Theory and Computation, 12(1):107–113, 2016. PMID: 26636615.

[50] David M. Bishop. Molecular vibrational and rotational motion in static and dynamic electric fields. Rev. Mod. Phys., 62:343–374, Apr 1990.

[51] A. Erba, M. T. Ruggiero, T. M. Korter, and R. Dovesi. Piezo-optic tensor of crystals from quantum-mechanical calculations. The Journal of Chemical Physics, 143(14):144504, 2015.

[52] M Jazbinšek and M. Zgonik. Material tensor parameters of $LiNbO_3$ relevant for electro- and elasto-optics. Applied Physics B, 74(4):407–414, 2002.

[53] A. Erba and R. Dovesi. Photoelasticity of crystals from theoretical simulations. Phys. Rev. B, 88:045121, Jul 2013.

[54] F. Pascale, C. M. Zicovich-Wilson, F. López Gejo, B. Civalleri, R. Orlando, and R. Dovesi. The calculation of the vibrational frequencies of crystalline compounds and its implementation in the crystal code. Journal of Computational Chemistry, 25(6):888–897, 2004.

[55] C. M. Zicovich-Wilson, F. Pascale, C. Roetti, V. R. Saunders, R. Orlando, and R. Dovesi. Calculation of the vibration frequencies of α-quartz: The effect of Hamiltonian and basis set. Journal of Computational Chemistry, 25(15):1873–1881, 2004.

[56] A. D. Becke. Density-functional thermochemistry. III. The role of exact exchange. The Journal of Chemical Physics, 98(7):5648–5652, 1993.

[57] C. Lee, W. Yang, and R. G. Parr. Development of the colle-salvetti correlation-energy formula into a functional of the electron density. Phys. Rev. B, 37:785–789, Jan 1988.

[58] J. P. Perdew, K. Burke, and M. Ernzerhof. Generalized gradient approximation made simple. Phys. Rev. Lett., 77:3865–3868, Oct 1996.

[59] C. Adamo and V. Barone. Toward reliable density functional methods without adjustable parameters: The PBE0 model. The Journal of Chemical Physics, 110(13):6158–6170, 1999.

[60] S. Dall'Olio, R. Dovesi, and R. Resta. Spontaneous polarization as a berry phase of the hartree-fock wave function: The case of $KNbO_3$. Phys. Rev. B, 56:10105–10114, Oct 1997.

[61] D. Vilela Oliveira, J. Laun, M. F. Peintinger, and T. Bredow. BSSE-correction scheme for consistent gaussian basis sets of double- and triple-zeta valence with polarization quality for solid-state calculations. Journal of Computational Chemistry, 40(27):2364–2376, 2019.

[62] R. P. McCall, E. M. Scherr, A. G. MacDiarmid, and A. J. Epstein. Anisotropic optical properties of an oriented-emeraldine-base polymer and an emeraldine-hydrochloride-salt polymer. Phys. Rev. B, 50:5094–5100, Aug 1994.

[63] L. Valenzano, B. Civalleri, S. Chavan, S. Bordiga, M. H. Nilsen, S. Jakobsen, K. P. Lillerud, and C. Lamberti. Disclosing the Complex Structure of UiO-66 Metal-Organic Framework: A Synergic Combination of Experiment and Theory. Chemistry of Materials, 23(7):1700–1718, apr 2011.

[64] Thomas Bredow, Karl Jug, and Robert A. Evarestov. Electronic and magnetic structure of $ScMnO_3$. physica status solidi (b), 243(2):R10–R12, 2006.

[65] D. Munoz Ramo, J. L. Gavartin, A. L. Shluger, and G. Bersuker. Spectroscopic properties of oxygen vacancies in monoclinic HfO_2 calculated with periodic and embedded cluster density functional theory. Phys. Rev. B, 75:205336, May 2007.

[66] See Supplemental Material at [] for more details on EO and second harmonic generation symmetry and complementary results on phonon modes of LNO and ZrO_2-HFO_2, crystal structure, and atomic positions.

[67] A. Dhar and A. Mansingh. Optical properties of reduced lithium niobate single crystals. Journal of Applied Physics, 68(11):5804–5809, 1990.

[68] C. Thierfelder, S. Sanna, Arno Schindlmayr, and W. G. Schmidt. Do we know the band gap of lithium niobate? Physica Status Solidi c, 7(2):362–365, 2010.

[69] H. H. Nahm and C. H. Park. First-principles study of microscopic properties of the Nb antisite in $LiNbO_3$: Comparison to phenomenological polaron theory. Phys. Rev. B, 78:184108, Nov 2008.

[70] U. Schlarb and K. Betzler. Refractive indices of lithium niobate as a function of wavelength and composition. Journal of Applied Physics, 73(7):3472–3476, 1993.

[71] J. G. Bergman, A. Ashkin, A. A. Ballman, J. M. Dziedzic, H. J. Levinstein, and R. G. Smith. Curie temperature, birefringence, and phase-matching temperature variations in $LiNbO_3$ as function of melt stoichiometry. Applied Physics Letters, 12(3):92–94, 1968.

[72] M. Veithen, X. Gonze, and P. Ghosez. First-principles study of the electro-optic effect in ferroelectric oxides. Phys. Rev. Lett., 93:187401, Oct 2004.

[73] D. F. Nelson and R. M. Mikulyak. Refractive indices of congruently melting lithium niobate. Journal of Applied Physics, 45(8):3688–3689, 1974.

[74] K. K. WONG. Properties of Lithium Niobate. (ISBN 0 85296 799 3):136, 2002.

[75] F. Abdi, M. Aillerie, P. Bourson, M. D. Fontana, and K. Polgar. Electro-optic properties in pure $LiNbO_3$ crystals from the congruent to the stoichiometric composition. Journal of Applied Physics, 84(4):2251–2254, 1998.

[76] P. Giannozzi, S. Baroni, N. Bonini, M. Calandra, R. Car, C. Cavazzoni, D. Ceresoli, G. L. Chiarotti, M. Cococcioni, and I. Dabo. *et al.*, QUANTUM ESPRESSO: A modular and open-source software project for quantum simulations of materials. Journal of Physics Condensed Matter, 21(39), 2009.

[77] R. Materlik, C. Kunneth, and A. Kersch. The origin of ferroelectricity in $Hf_{1-x}Zr_xO_2$: A computational investigation and a surface energy model. Journal of Applied Physics, 117(13), 2015.

[78] M. Materano, P. Reinig, A. Kersch, M. Popov, M. Deluca, T. Mikolajick, U. Boettger, and U. Schroeder. Raman Spectroscopy as a Key Method to Distinguish the Ferroelectric Orthorhombic Phase in Thin ZrO_2 Based Films. Physica Status Solidi (RRL) – Rapid Research Letters, 16(4):2100589, 2022.

[79] A. Yariv and P. Yeh. Photonics: Optical electronics in modern communications. Oxford University Press, 6 edition, 2007.

[80] E. H. Kisi and C. J. Howard. Crystal structures of zirconia phases and their inter-relation. Key Engineering Materials, 154(153-154):1–36, 1998.

[81] E. H. Kisi. Influence of hydrostatic pressure on the t→o transformation in mg-psz studied by in situ neutron diffraction. Journal of the American Ceramic Society, 81(3):741–745, 1998.

[82] Iris Inbar and R. E. Cohen. Comparison of the electronic structures and energetics of ferroelectric $LiNbO_3$ and $LiTaO_3$. Phys. Rev. B, 53:1193–1204, Jan 1996.

[83] V. Caciuc, A. V. Postnikov, and G. Borstel. Ab initio structure and zone-center phonons in $LiNbO_3$. Phys. Rev. B, 61:8806–8813, Apr 2000.

[84] Seiji Kojima. Composition variation of optical phonon damping in lithium niobate crystals. Japanese Journal of Applied Physics, 32(Part 1, No. 9B):4373–4376, sep 1993.

[85] R. Claus, J. Brandmüller, G. Borstel, E. Wiesendanger, and L. Steffan. Directional Dispersion and Assignment of Optical Phonons in $LiNbO_3$. Zeitschrift für Naturforschung A, 27(8-9):1187–1192, 1972.